Characterization of a neutron imaging setup at the INES facility

(Article begins on next page)

03 May 2024

UNIVERSITÀ DEGLI STUDI DI TORINO

CHARACTERIZATION OF A NEUTRON IMAGING SETUP AT THE INES FACILITY

E. A. DURISI[1,2*], L. VISCA[1,2], F. ALBERTIN[2], R. BRANCACCIO[2], J. CORSI[1,2], G. DUGHERA[2], , W. FERRARESE[1,2], A. GIOVAGNOLI[3], N. GRASSI[3], F. GRAZZI[4], A. LO GIUDICE[1,2], G. MILA[1,2], M. NERVO[3], N. PASTRONE[2], F. PRINO[2], L. RAMELLO[5,2], A. RE[1,2], A. ROMERO[1,2], R. SACCHI[1,2], F. SALVEMINI[4], A. SCHERILLO[4,6], A. STAIANO[2]

[1]*Università di Torino, Dipartimento di Fisica, Via Pietro Giuria 1, 10125 Torino, Italy*
[2]*Istituto Nazionale di Fisica Nucleare – Sezione di Torino, Via Pietro Giuria 1, 10125 Torino, Italy*
[3]*Fondazione Centro per la Conservazione ed il Restauro dei Beni Culturali "La Venaria Reale", Piazza della Repubblica, 10078 Venaria Reale (Torino), Italy*
[4]*Consiglio Nazionale delle Ricerche, Istituto dei Sistemi Complessi, Via Madonna del Piano 10, 50019 Sesto Fiorentino (Firenze), Italy*
[5]*Università del Piemonte Orientale, Dipartimento di Scienze e Innovazione Tecnologica, Viale Teresa Michel 11, 15121 Alessandria, Italy*
[6]*Science and Technology Facility Council, ISIS Neutron Source - Didcot, United Kingdom*

*Corresponding author at: Università di Torino, Dipartimento di Fisica, Via Pietro Giuria 1, 10125 Torino, Italy, Phone: +390116707954, Fax: +390116707020
e-mail address: elisabettaalessandra.durisi@unito.it

ABSTRACT

The Italian Neutron Experimental Station (INES) located at the ISIS pulsed neutron source (Didcot, United Kingdom) provides a thermal neutron beam mainly used for diffraction analysis. A neutron transmission imaging system was also developed for beam monitoring and for aligning the sample under investigation. Although the time-of-flight neutron diffraction is a consolidated technique, the neutron imaging setup is not yet completely characterized and optimized. In this paper the performance for neutron radiography and tomography at INES of two scintillator screens read out by two different commercial CCD cameras is compared in terms of linearity, signal-to-noise ratio, effective dynamic range and spatial resolution. In addition, the results of neutron radiographies and a tomography of metal alloy test structures are presented to better characterize the INES imaging capabilities of metal artifacts in the cultural heritage field.

Keywords: Neutron imaging; Metal alloy; Cultural heritage

1. Introduction

Analysis techniques based on thermal and epithermal neutrons represent a powerful tool to characterize metal alloy artifacts in the cultural heritage field. Neutrons are a non-invasive diagnostic tool and can penetrate thick layers of samples. Neutron transmission imaging, obtained with radiographic or

39 tomographic techniques, allows to investigate the inner structure of artworks,
40 determining, as an example, the materials thickness and the conservation
41 condition [1, 2]. All this information can be helpful to assist restoration activities,
42 to increase the knowledge of the work of art and to help dating or attributing an
43 artifact through the understanding of the manufacturing techniques used.
44 The Italian Neutron Experimental Station (INES) is a neutron diffractometer
45 located at the ISIS pulsed neutron source [3]. A low-cost imaging device is
46 currently installed and used for beam monitoring and samples positioning.
47 Preliminary measurements were performed by Bartoli et al. [4] to test the imaging
48 setup. Salvato et al. realized an upgrade of the system providing the first neutron
49 tomography investigation at INES [5].
50 The aim of this paper is to fully characterize the present imaging setup in terms of
51 linearity, signal-to-noise ratio, effective dynamic range and spatial resolution. A
52 comparison with a different converter screen and a different CCD camera will be
53 shown. Moreover, the analysis of neutron radiography and tomography of metal
54 alloy test structures will be presented in order to assess the diagnostic potential of
55 the INES imaging apparatus on metal artifacts in the cultural heritage field.
56

2. Experimental set up

58 The Italian Neutron Experimental Station, INES, provides a stable pulsed neutron
59 beam with an approximately uniform intensity distribution over a cross section, at
60 the sample position, of 35x35 mm^2 (40x40 mm^2 including also non-uniform
61 borders). The divergence of the beam, in terms of L/D ratio, is about 90.
62 The neutron imaging setup currently installed consists of a scintillator converter
63 screen, a mirror and a commercial CCD camera [6]. The scintillator is made of
64 ZnS/^{6}LiF, 225 μm thick, layered on an aluminum substrate; in the following we
65 will refer to it as scintillator 1. It is positioned orthogonal to the incident neutron
66 beam, at a distance from the sample ranging from 1 cm to 10 cm and it emits
67 visible light centered at a wavelength of about 520 nm, in order to best match the
68 CCD sensitivity curve. A mirror reflects the emitted light toward a black and
69 white camera (The Imaging Source DMK21BF04) equipped with an optical
70 system of f=16mm and F/1.4. The camera works at room temperature without any
71 image intensifier and is based on a Sony ICX098BL CCD sensor with 640x480

72   pixels of 5.6 μm size, one pixel corresponding to 100 μm in the image field, read

73   out by a 10 bit ADC whose most significant 8 bits encode the CCD output signal.

74   In order to test how the performance depends on the components of the existing

75   system, a second converter screen, named scintillator 2 in the following, and a

76   different CCD camera were also tested. The converter has the same composition

77   as scintillator 1, embedded in a stable plastic matrix, and has a total thickness of

78   450 μm. The CCD camera is a Manta G-032B (Allied Vision Technology)

79   equipped with the same optical system of f=16 mm and F/1.4. The CCD sensor is

80   a Sony ICX424 with 656x492 pixel of 7.4 μm size, one pixel corresponding to

81   100 μm in the image field, read out by a 12 bit ADC.

82   An x-y translator, positioned inside the sample tank, is available for sample

83   alignment [6]. A precision rotary stage (Newport URS150-BPP) was added to the

84   existing setup to perform a neutron tomography.

85   In order to test the diagnostic potential of the apparatus on metal artifacts, test

86   samples were prepared by the INFN (National Institute of Nuclear Physics)

87   mechanical workshop in Torino. The densities and material compositions of these

88   samples are reported in Table 1.

89   In particular, to probe the imaging capabilities of the apparatus as a function of

90   material composition and thickness, three step wedges of steel, brass and

91   quaternary bronze alloy were prepared (figure 1 a). These three materials were

92   chosen as they constitute by far the most common metal alloys used in the past for

93   cultural artifacts. Each step is a square of 10x10 mm^2 with a thickness

94   incrementing in each step by 2 mm, from 2 mm up to a maximum of 30 mm. In

95   addition, to investigate the capability of neutron tomography of metal alloy

96   objects, a 25 mm edge bronze cube (figure 1 b) was built to fit in the spot size of

97   the INES neutron beam. The cube faces are held together by means of screws and

98   welds and have a thickness of 4 mm, reduced to 2 mm for two opposite side faces,

99   to mimic the typical bronze thicknesses of statues. Two circular holes of 1 mm

100 diameter were added on one of the two thinner faces to simulate air bubbles and

101 three square base rods, 3x3x15 mm^3 size, two made of steel and one of aluminum,

102 were inserted in the central part to simulate the presence of inner structures.

3. Results

The two scintillator screens coupled with both the CCD cameras were tested in order to determine the linearity, the signal-to-noise ratio, the effective dynamic range and the spatial resolution separately for all the combinations. Later, the best combinations were used to analyze the metallic test samples.

3.1 Linearity

For this, a set of images of the light emitted by the converter screen illuminated by the open neutron beam was collected for increasing exposure times to simulate the behavior with increasing signal intensities. A square region of interest (ROI) of 10x10 pixels, corresponding to an area of approximately 1 mm^2 of the image field, was selected in the central area of the images, where the neutron beam is uniform, and was used to calculate the average ADC value (or gray level) and its standard deviation (or noise). These quantities are derived with the assumption that the pixels gray level fluctuations in the ROI of a single image are equivalent to the gray level fluctuations of a single pixel in a sequence of identical images.

The measurements with the DMK camera, with both the scintillator screens, were performed by setting the electronic gain to 24.6 dB (available range is 0 - 36 dB) and increasing the exposure times up to the maximum allowed of 30 s. Similar measurements with the Manta camera were performed setting the electronic gain to 15 dB (available range is 0 dB- 36 dB) and increasing the exposure time up to the maximum available of 60 s. The results are shown in figure 2 and 3 where the gray levels are displayed as a function of the exposure time. It should be noticed that, at the maximum exposure time, the signal range of the DMK camera covers only about one half of the available 256 gray levels. On the contrary, at the maximum exposure time, the Manta camera reaches with the scintillator 2 the saturation level of 4095; this value is therefore not included in the analysis.

The data indicate a good linearity of the imaging systems as resulting from the fits to a straight line shown in the figures 2-3, the maximum deviation from linearity being 1 gray level for DMK with both scintillators and 25 and 12 gray levels for Manta with scintillator 1 and scintillator 2 respectively. In addition, the slope of the fit for the thicker converter, scintillator 2, is always larger, as expected as a consequence of the larger conversion efficiency. For a fixed exposure time this

136 leads to a slightly larger effective dynamic range, as will be shown in the
137 following section.

138

3.2 Effective dynamic range

140 First the signal-to-noise ratio was studied, where the signal and the noise were
141 determined for increasing exposure times as described in the previous section. It is
142 found that, for all the different setup configurations, the signal-to-noise ratio as a
143 function of the gray level signal can be approximated by a power curve with a
144 fractional exponent; an example it is shown in figure 4 for the Manta camera
145 coupled with scintillator 2. This behavior indicates that the dominant contribution
146 to the noise is originated from the statistical fluctuations in the number of photons
147 hitting the CCD cells and thus increases with the signal level; in fact, assuming a
148 pure Poisson statistical process, the signal-to-noise ratio should behave like a
149 power function with exponent equal to 0.5.

150 In order to compare the effective dynamic range of the different combinations of
151 camera and converter, the method described in [8] was used. The effective
152 dynamic range can be expressed as the number of effective distinguishable gray
153 levels L of the system, depending on both the signal s and the noise $N(s)$, through
154 the formula

155
$$L = \int \frac{ds}{N(s)} \tag{1}$$

156 where the integration is performed over the useful signal range. Since this range
157 increases with the exposure time and given the poissonian nature the noise, the
158 comparison should be performed for equal exposure times, i.e. for equal number
159 of neutrons hitting the converter, and the signal integration ranges should be
160 chosen accordingly.

161 As an example, figure 5 shows 1/noise as a function of the gray level for the same
162 camera and scintillator of figure 4. For each scintillator-camera combination the
163 data were fitted with a power function and, for each exposure time, the result was
164 integrated from dark signal (8.33 and 9.13 gray levels for DMK and Manta
165 respectively) up to the measured signal level shown in the figures 2 and 3.

166 The results are shown in figure 6 where the effective number of gray levels L is
167 represented as a function of the exposure time. For each exposure time the
168 scintillator 2 is providing a slightly better dynamic range than the scintillator 1

169 and so does the Manta camera compared to the DMK. The best combination is
170 found to be the Manta CCD camera coupled with scintillator 2 which reaches
171 about 80 effective gray levels before saturation. On the contrary the present INES
172 imaging system comprising the DMK camera is limited in dynamic range mainly
173 because of the shorter maximum exposure time of the camera. Table 2
174 summarizes the maximum dynamic ranges, corresponding to the maximum
175 exposure time before saturation, expressed for all the combinations both in terms
176 of effective number of gray levels L and in dB through the formula

177
$$D(dB) = 20\log L \tag{2}$$

178 It should be observed that even if these results were obtained in a limited central
179 area of the image of 1 mm^2, their validity can be extended to the entire beam
180 active area as the maximum non-uniformity was measured to be below 1% (5%)
181 sampling a region of 1 mm^2 in a central area of 24x24 mm^2 (35x35 mm^2).

182

183 **3.3 Spatial resolution**

184 The spatial resolution of the radiographic system was evaluated by analyzing the
185 image of a high contrast sharp edge, realized with a Gadolinium slab, in terms of
186 the Edge Spread Function (ESF) and the Modular Transfer Function (MTF) [9].
187 The edge was placed at around 10 cm far from the scintillator in order to
188 reproduce the measurement conditions required in the tomography set-up. Since
189 the Gd slab was not perfectly aligned with the CCD, the sharp edge image was
190 fitted with a modified Cauchy functional form:

191
$$\varphi(x,y)_{a,b,\beta,\lambda,x_0} = a\left\{\frac{1}{2} + \frac{1}{\pi}\arctan[\lambda(x - \beta y - x_0)]\right\} + b \tag{3}$$

192 where a and b are constants, x and y are the coordinates in the image plane, x_0 is
193 the edge position, β is the edge slope and λ is a parameter related to the full width
194 half maximum (FWHM) of the ESF derivative. In fact it can be shown that

195
$$\text{FWHM} = \frac{2}{\lambda}\cos(\tan^{-1}\beta) \approx \frac{2}{\lambda}\left(1 - \frac{\beta^2}{2}\right) \tag{4}$$

196 where the last approximation is valid for small values of β.
197 The spatial resolution FWHM obtained with this method for all combinations of
198 CCD cameras and scintillators is summarized in Table 3.
199 The corresponding MTF was obtained from the ESF derivative by Fourier
200 transform and the spatial frequency corresponding to the MTF value of 0.1 was

201 considered as the spatial resolution of the imaging system in lp/mm. The results
202 are summarized in Table 4.
203 As expected, the scintillator 1, being thinner than scintillator 2, shows a better
204 spatial resolution. It is also found that the spatial resolution of the Manta camera
205 appears worse than with the DMK; this can be partially explained by considering
206 that the optical system used for the experiment was specifically optimized for the
207 use with the DMK camera.

208

209 **3.4 Study of the test samples**

210 In order to test the imaging capabilities of the apparatus as a function of metal
211 type and thickness, neutron radiographies of the three step wedges made of steel,
212 brass and quaternary bronze alloy were acquired. Additional dark and open beam
213 images were acquired for later correction. Only the Manta CCD camera coupled
214 with scintillator 2 was used in order to exploit the highest effective dynamic
215 range. Images were acquired setting the integration time to 45 s to avoid
216 saturation effects, and the electronic gain to 15 dB.

217 To reduce the randomly distributed noise due to scattered gamma rays, the raw
218 images were processed with a radius 3 median filter [10]. The final positive
219 radiographic image (I_F) was obtained by subtracting from the raw image (I) the
220 dark image (D) and normalizing to the beam image (B) to correct for the
221 inhomogeneities of the beam, according to the formula:

222
$$I_F = \frac{(I) - (D)}{(B) - (D)} \tag{5}$$

223 Figure 7 shows the radiographic image of the three step wedges and the
224 corresponding gray level profiles, calculated averaging over 20 rows of pixels in
225 the centre of the wedge. Here, zero level corresponds to complete absorption
226 (black) and one to no absorption (white). Given the good linearity of the system,
227 the profiles can also be interpreted as neutron beam intensity profiles. As
228 expected, for all the three wedges, the gray level of each step decreases with the
229 increase of the thickness (right to left in the figure), up to the largest thickness
230 where the noise contribution starts to dominate. It can be deduced from this figure
231 that only those metallic art objects having a metal thickness not exceeding 30 mm
232 can be conveniently investigated with this system. The separation among the three
233 profiles originates from the differences of the neutron cross sections for the

234   different wedge materials. For reference, figure 8 displays the total cross sections

235   of the three constituent materials as a function of the neutron energy calculated

236   with the MCNP4C2 simulation code [11] in the INES neutron energy range (7.8

237   meV – 5 eV). Such a difference in the cross section, combined with a 3D

238   tomographic reconstruction, could be exploited to differentiate the constituting

239   metal of hidden parts of the object.

240   Figure 9 shows, for each of the three wedges, the attenuation of the neutron beam

241   as a function of the thickness of the wedge step. Since the intensity I of a neutron

242   beam traversing a material thickness x is attenuated according to the exponential

243   law $I = I_0 e^{-\Sigma x}$, it is possible by performing a fit to extract the macroscopic cross

244   section Σ separately for the three materials. Table 5 shows the results in terms of

245   cross section over density (Σ/ρ) compared to the predictions obtained by

246   processing the ENDF/B VI microscopic cross sections with the MCNP4C2 code

247   and extracting the expected Σ at the neutron beam energy of 1 eV; this energy

248   corresponds to the average of the INES beam energy spectrum at the sample

249   position [3]. The agreement is found to be satisfactory within the statistical

250   uncertainty.

251   Finally, in order to investigate the potential of neutron tomography on metal alloy

252   objects, a tomography of the bronze cube was performed. Here the DMK camera

253   and the scintillator 1 were used as they showed to provide the best spatial

254   resolution. The cube, placed 10 cm far from the scintillator screen, was rotated by

255   angular steps of 0.7° up to a total of 179.9° and a projection was acquired at each

256   angular position using an exposure time of 16 s.

257   To perform the 3D volume reconstruction, the algorithm of Filtered Back-

258   Projection (FBP), developed for X-ray tomography and implemented in the

259   Imgrec software [12], was used. Parallel beam geometry was assumed which

260   allows the reconstruction using projections over 180° [13].

261   The tomography of the cube proved the possibility to resolve details at a

262   millimetric scale inside metal structures. Figure 10 shows a horizontal section and

263   a 3D rendering of the cube. Welds and holes are clearly visible in the horizontal

264   section. Note that in the figure the aluminum column is invisible as the aluminum

265   cross section is about one order of magnitude lower than steel cross section.

266   However, changing the gray level threshold, the 3D rendering of the cube worsens

267   but the aluminum column becomes visible.

4. Conclusions

Series of measurements were performed to characterize the imaging capabilities of the INES setup for objects of interest in the cultural heritage field. Different combinations using a thicker scintillator screen and a different CCD camera with a larger maximum bit depth were also tried to find possible improvements to the existing system.

For all the combinations a good linearity of the imaging system was obtained. The best dynamic range of about 80 effective gray levels was obtained with a Manta 12 bit CCD camera coupled with the thicker scintillator. On the contrary the present INES imaging system, comprising a DMK 8 bit CCD camera and the thinner scintillator, was limited to about 43 effective gray level mainly because of the short maximum exposure time of this camera. However this combination showed the best spatial resolution of 182 μm (FWHM), corresponding to 4.0 lp/mm.

The combination featuring the best dynamic range was used to investigate the imaging capabilities for metal alloy objects as a function of the metal thickness and alloy composition. For this purpose, three step wedges made of steel, brass and bronze were analyzed, showing that the investigation of metallic objects up to a thickness of about 30 mm can be achieved at this facility. The neutron attenuation coefficients for the three metal alloys were also measured from the attenuation curves and compared with the predictions of the ENDF/BVI library, showing a good agreement.

Finally, the tomography of a hollow bronze cube with wall thicknesses in the range 2-4 mm, typical of the bronze statues, and with inner insertions of steel and aluminum parts, was carried on using the present INES setup in order to exploit the best spatial resolution. The results showed that the presence of metallic structures inside the bronze shell can be easily revealed with this technique, and that holes and welding material at a millimetric scale can be revealed.

Acknowledgements

References

1 Lehmann E H et al. Nuclear Instruments and Methods in Physics Research A "Non-invasive studies of objects from cultural heritage" (2005), 542 68–75.

2 Lehmann E H et al. Archaeometry "Investigation of the content of ancient Tibetan metallic Buddha statues by means of neutron imaging methods" (2010) 52, 3:416-428.

3 Grazzi F et al. Nuovo Cimento "Preliminary results of the Italian neutron experimental station INES at ISIS: Archaeometric applications" (2007) 30 59-65.

4 Bartoli L et al. Nuclear Instruments and Methods in Physics Research A "Test measurements with a new imaging alignment camera at ISIS" (2008) 595, 643-646.

5 Salvato G et al. Nuovo Cimento "Neutron Tomography at INES: first experimental results" (2008) 31 C, N. 4.

6 Grazzi F et al. Review of Scientific Instruments "A neutron imaging device for sample alignment in a pulsed neutron scattering instrument" (2009) 80 1-4.

7 Data provided by the material supplier.

8 Bettuzzi M et al. Proceedings of SPIE "Effective dynamic range measurement for a CCD in full-field industrial X-ray imaging applications" (2007) 6616 66161L.

9 Hall E L "Computer image processing and recognition" (1979) Academic Press, New York.

10 http://rsb.info.nih.gov/ij/

11 Briesmeister J F E "MCNP—a general Monte Carlo N-particle transport code" Version 4C, LA-13709 (2000) Los Alamos National Laboratory Report.

12 Developed by D Schneberk at Lawrence Livermore National Laboratory, see also Martz H E et al. "X-ray Imaging" (2009) CRC Press Inc, Bosa Roca.

13 Kak A C and Slaney M "Principles of Computerized Tomographic Imaging" (1988), IEEE Press.

Figures Captions

Fig. 1 The three step wedges (a) and the bronze cube (b).

Fig. 2 DMK camera: linearity of the signal as a function of the exposure time.

Fig. 3 Manta camera: linearity of the signal as a function of the exposure time.

Fig. 4 Manta camera: signal to noise ratio as a function of the gray level signal.

Fig. 5 Manta camera: 1/noise as a function of the gray level.

Fig. 6 Effective number of gray levels as a function of the exposure time for the four different combinations of camera and converter.

Fig. 7 Neutron radiography of the three step wedges (above) and corresponding neutron absorption profiles (below). The upper scale of the plot indicates the step thickness.

Fig. 8 Total neutron cross sections of the constituent materials of the step wedges calculated with MCNP4C2 simulation code.

Fig. 9 Neutron attenuation curves for the three wedges as a function of the step thickness.

Fig. 10 Cube phantom tomography reconstruction: section (a) and 3D rendering (b).
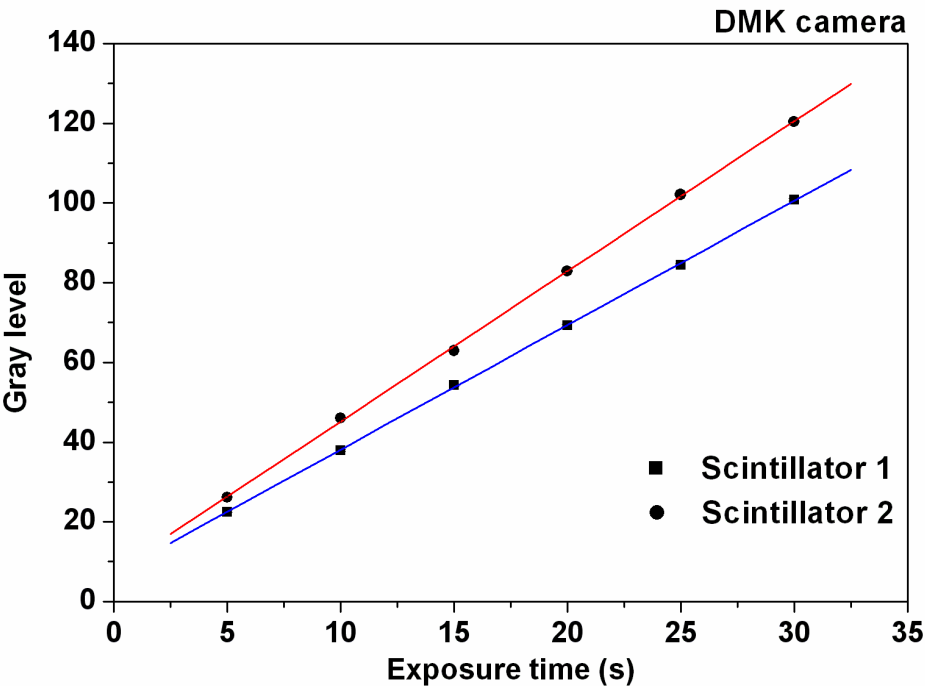
361 **Figure 1**
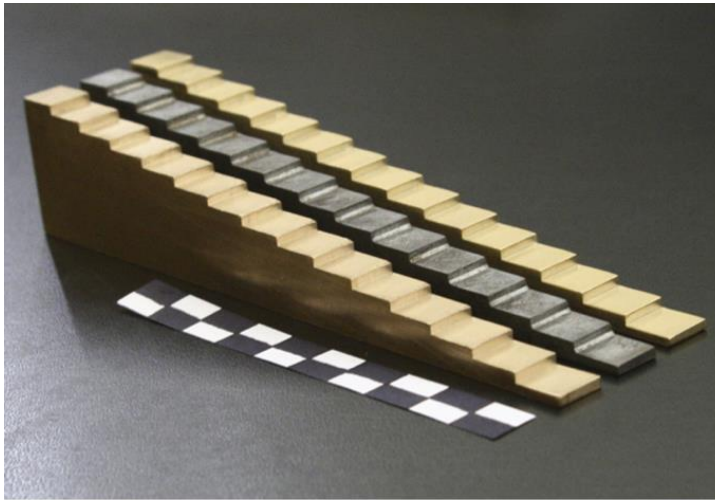
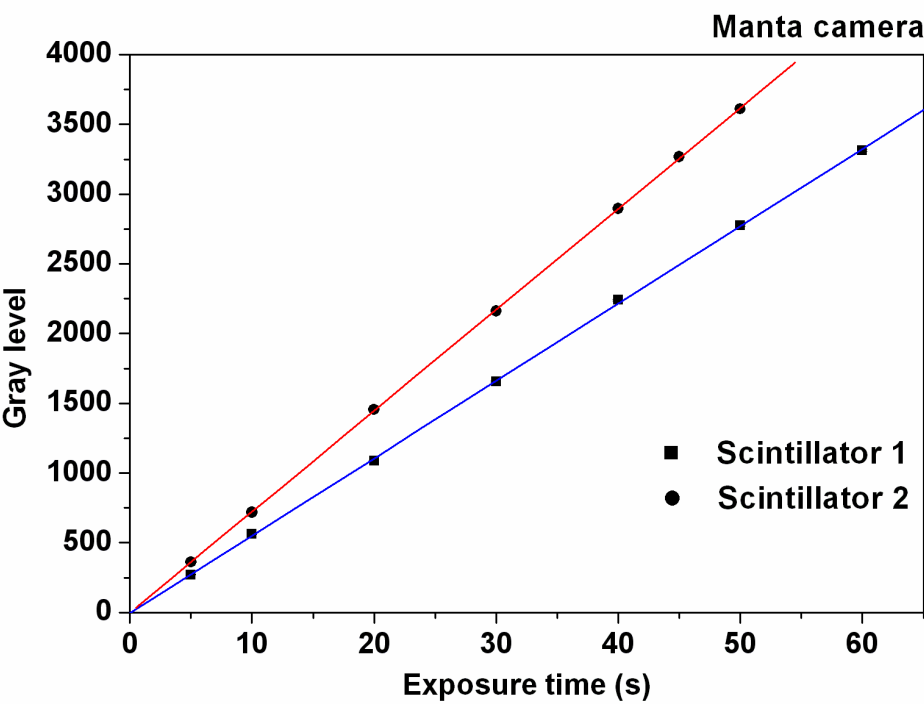*(a)*   *(b)*
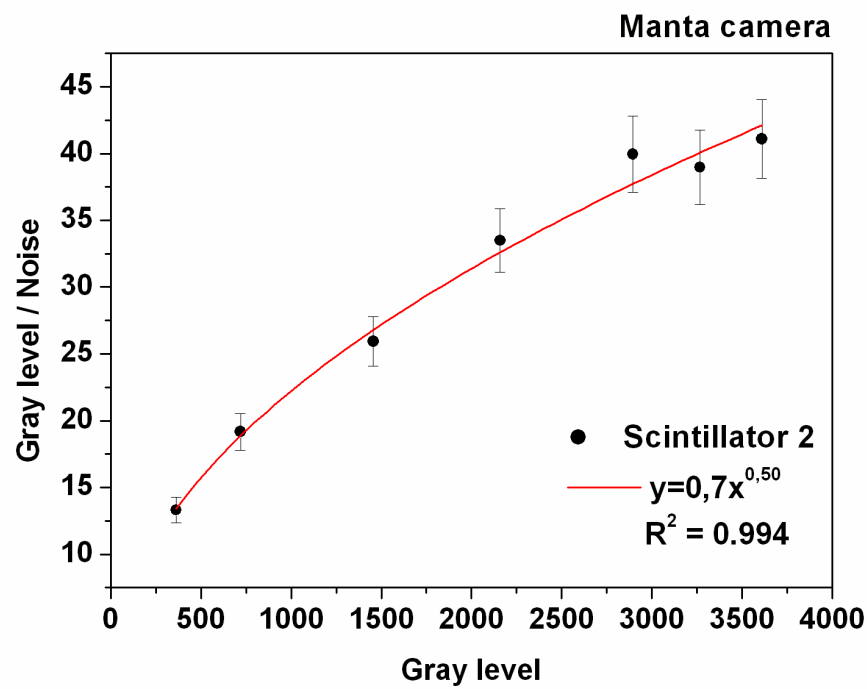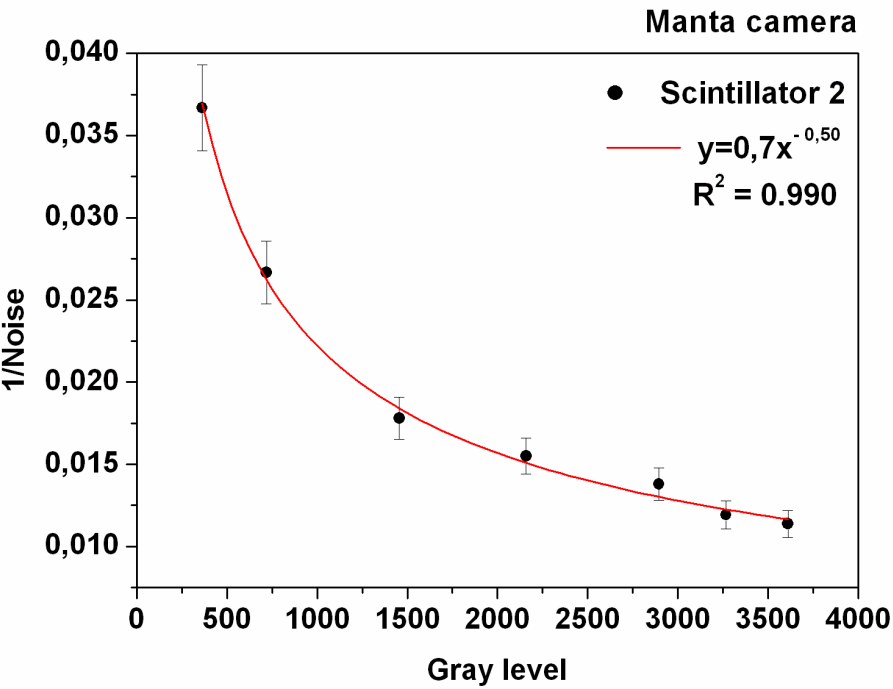
362
363

364 **Figure 2**

365

366

367   **Figure 3**

370   **Figure 4**

Manta camera

371
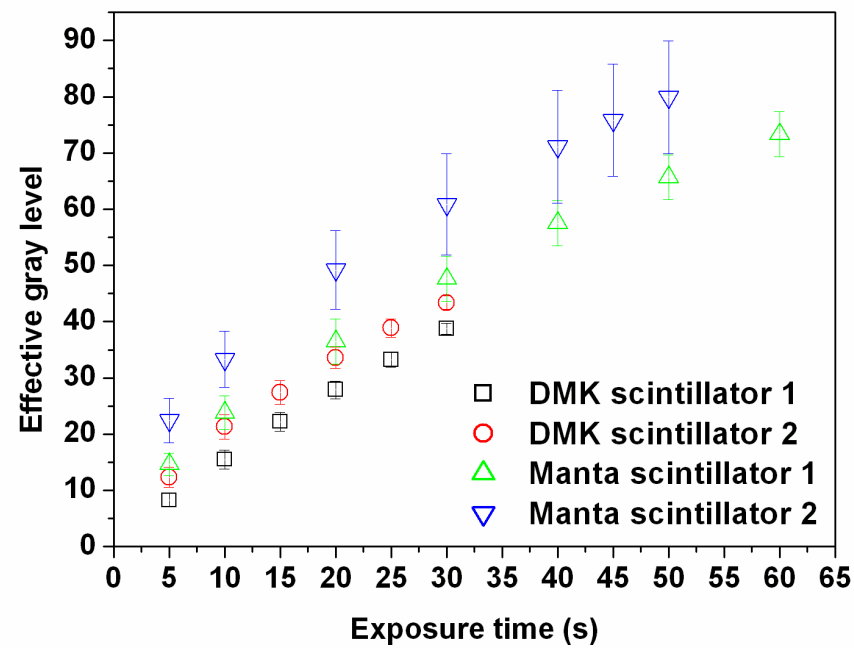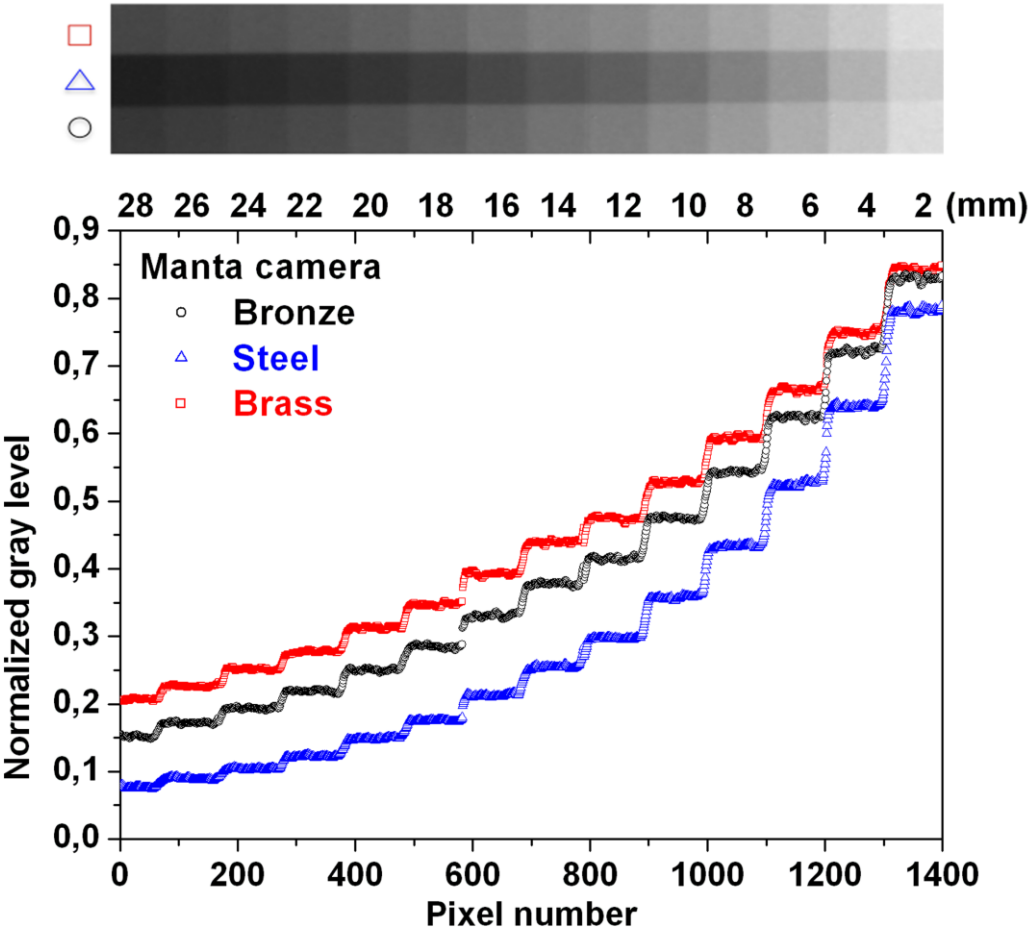
372   **Figure 5**

373

374
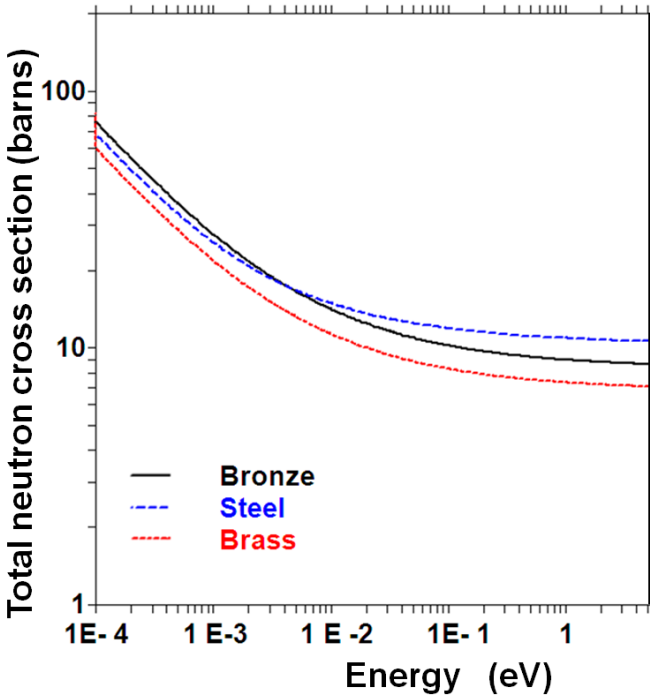
375   **Figure 6**

376
377

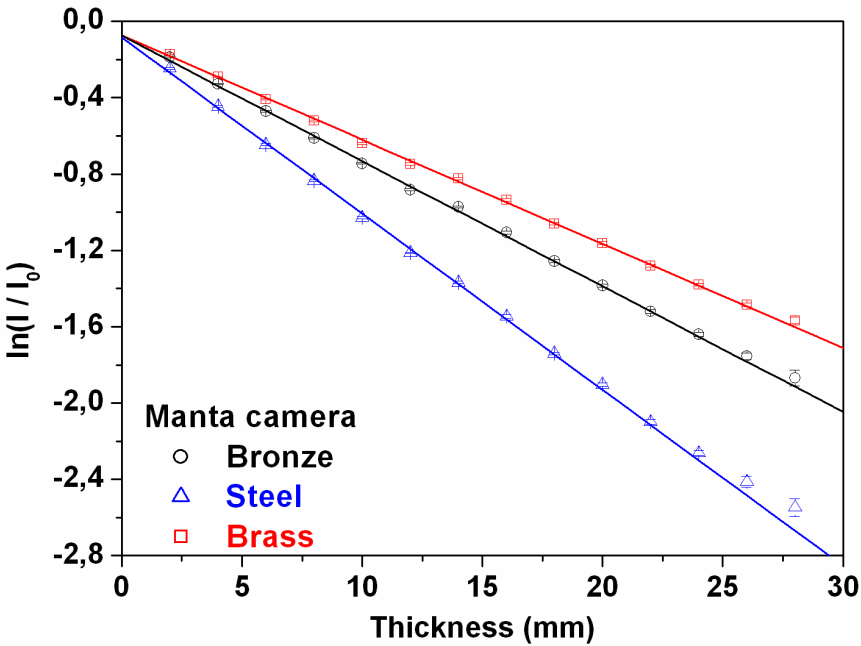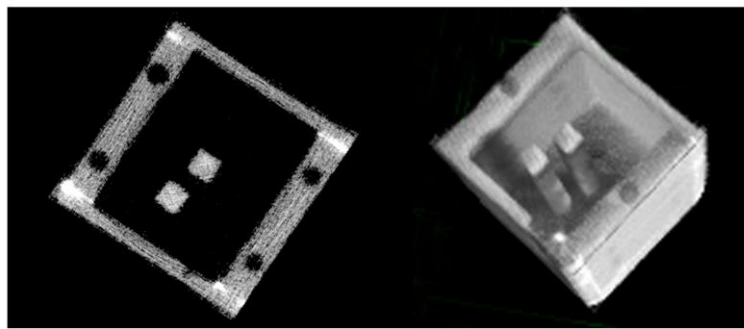378 **Figure 7**

381   **Figure 8**

382

383

384   **Figure 9**

385

386

387 **Figure 10**

(a)　　　　　*(b)*

388
389
390

391   Table1: Samples density and elemental composition [7].

392

Material	Density [g cm^{-3}]	Elemental composition
C40 carbon steel	7.85	Fe; C (0.38-0.43%); Si (0.15-0.35%); Mn (0.6-0.8%); P (max 0.02%); S (max 0.008%); Cr (0.15-0.35%)
Turning brass	8.29	Cu; Zn (39%); Pb (3%)
Bronze (85-5-5-5)	8.88	Cu; Pb (5.81%); Sn (5.05%); Zn (5.46 %); Fe (0.11%); Ni (1.21%); Al (trace)

393

394

395

396   Table 2: Maximum effective dynamic range in terms of effective number of gray

397   levels and in dB.

	DMK		Manta	
Scintillator 1	39±2	(31.8±0.4) dB	73±4	(37.3±0.5) dB
Scintillator 2	43±1	(32.7±0.2) dB	80±10	(38.1±1.1) dB

398

399

400

401   Table 3: Spatial resolution, defined as FWHM of the ESF derivative, measured for

402   both cameras coupled with both scintillators.

FWHM (μm)	DMK	Manta
Scintillator 1	182±11	261±9
Scintillator 2	306±14	389±13

403

404

405   Table 4: Spatial resolution defined as MTF value at 10% calculated for both

406   cameras coupled with both scintillators.

407

MTF 10% (lp/mm)	DMK	Manta
Scintillator 1	4.0±0.2	2.74±0.10
Scintillator 2	2.37±0.11	1.84±0.06

408

409   Table 5: Σ/ρ values obtained with Manta CCD camera compared to the

410   predictions.

411

Material	ρ (g cm^{-3})	Measured Σ/ρ (cm^2 g^{-1})	ENDF/B-VI Σ/ρ @1 eV (cm^2 g^{-1})
Steel	7.85	$(11.9\pm0.4)\ 10^{-2}$	$12.02\ 10^{-2}$
Brass	8.29	$(6.6\pm0.2)\ 10^{-2}$	$6.64\ 10^{-2}$
Quaternary bronze alloy	8.88	$(7.4\pm0.2)\ 10^{-2}$	$7.24\ 10^{-2}$

412

413